


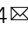





A Fe₃N/carbon composite electrocatalyst for effective polysulfides regulation in room-temperature Na-S batteries

Yuruo Qi^{1,5}, Qing-Jie Li^{2,5}, Yuanke Wu¹, Shu-juan Bao¹, Changming Li¹ , Yuming Chen^{2,3} , Guoxiu Wang⁴   & Maowen Xu¹  

The practical application of room-temperature Na-S batteries is hindered by the low sulfur utilization, inadequate rate capability and poor cycling performance. To circumvent these issues, here, we propose an electrocatalyst composite material comprising of N-doped nanocarbon and Fe₃N. The multilayered porous network of the carbon accommodates large amounts of sulfur, decreases the detrimental effect of volume expansion, and stabilizes the electrodes structure during cycling. Experimental and theoretical results testify the Fe₃N affinity to sodium polysulfides via Na-N and Fe-S bonds, leading to strong adsorption and fast dissociation of sodium polysulfides. With a sulfur content of 85 wt.%, the positive electrode tested at room-temperature in non-aqueous Na metal coin cell configuration delivers a reversible capacity of about 1165 mA h g⁻¹ at 167.5 mA g⁻¹, satisfactory rate capability and stable capacity of about 696 mA h g⁻¹ for 2800 cycles at 8375 mA g⁻¹.

¹Key Laboratory of Luminescence Analysis and Molecular Sensing, Ministry of Education, Faculty of Materials and Energy, Southwest University, Chongqing 400715, PR China. ²Department of Nuclear Science and Engineering, Massachusetts Institute of Technology, Cambridge, MA 02139, USA. ³College of Environmental Science and Engineering, Fujian Normal University, Fuzhou 350007, PR China. ⁴Center for Clean Energy Technology, University of Technology Sydney, Sydney, NSW 2007, Australia. ⁵These authors contributed equally: Yuruo Qi, Qing-Jie Li. email: yumingc126@126.com; Guoxiu.Wang@uts.edu.au; xumaowen@swu.edu.cn

Room-temperature sodium–sulfur (RT Na–S) batteries hold significant promise for large-scale application due to the abundance, nontoxicity, low cost and high theoretical capacity of both electrodes (Na anode and S cathode)^{1–3}. Similar to Li–S batteries, Na–S batteries are also facing several challenges, such as low sulfur loading, unsatisfactory reversible capacity, inadequate rate capability, and rapid capacity fading^{1–3}. These problems are typically triggered by the following intractable issues, which include the insulating nature of sulfur and its discharged products, the sluggish electrochemical reactivity of solid sulfur with sodium, the high solubility of polysulfides in the electrolyte^{4–6} and the huge volume expansion during the discharge/charge process.

In attempting to address these problems, constructing hierarchical sulfur hosts is highly desirable. Nanocarbons^{7–9} with excellent electronic conductivity and large surface areas are employed to balance the inferior electronic conductivity of sulfur and physically confine sodium polysulfides (NaPSs). However, the nonpolar feature of these carbon materials signifies insufficient mutual interaction to completely eliminate the shuttling of polysulfides. Subsequently, polar materials with intrinsic affinity to sulfur/polysulfides are introduced to anchor polysulfides chemically and thus enhance the cycling stability. Recently, electrocatalysts (including metals, metal oxides, metal sulfides, etc.) are proposed to accelerate the conversion kinetics of polysulfides and suppress the shuttling of polysulfides based on the strong catalytic activity^{10–12}. Metal nitrides, featured with low cost, excellent chemical stability, good conductivity, and strong adhesion to polysulfides, have been widely investigated in Li–S batteries^{13–15}; however, such metal nitrides have been rarely applied in RT Na–S batteries and their effectiveness and associated mechanisms in RT Na–S batteries remain unclear.

A further issue for most reported studies is the low sulfur content which could hinder the practical application. As Na–S batteries development is in its infancy, the attention to increase sulfur loading of Na–S cathodes is still insufficient. It has been acknowledged that 70% sulfur loading is critical to achieve high-energy-density Li–S batteries^{16–19}. Being on a par with the energy density of Li–S batteries, a sulfur loading more than 70% in Na–S batteries is indispensable due to the larger atomic mass of Na. However, without proper cathode design, the massive load of sulfur will form a thick insulating layer, which eventually reduces the utilization rate and reaction kinetics. What's worse, the notorious shuttle effect of NaPSs will be exacerbated and result in worse cycling stability. Therefore, it is an urgent need to explore the rational design of hierarchical cathodes, which can synergistically inhibit the shuttle of NaPSs and enhance the electrochemical reactivity of sulfur with sodium under high-sulfur content.

In this research work, we propose a highly efficient Fe₃N catalyst on N-doped multilayered carbon networks (NMCN) that enables strong adsorption and fast dissociation of NaPSs for advanced Na–S batteries. The NMCN featured with a hierarchical pore structure can accommodate massive sulfur, suppress volume expansion, and stabilize the cycling process. As far as we know, there has been no previous study employing nitrides in cathode hosts for Na–S batteries. The as-prepared S@Fe₃N-NMCN cathode can be directly used as a freestanding electrode without any other binders, conductive additives and current collectors, which significantly reduces the time and cost for assembling the battery. Both the pores within nanofibers and the interstice between layers can provide adequate space for sulfur loading. Fe₃N shows prominent affinity to NaPSs via Na–N and Fe–S bonding, leading to efficient NaPSs dissociation. Benefiting from these structural and compositional advantages, a high-sulfur loading of 85wt.% (2.6 mg cm⁻²) is achieved. Importantly, the S@Fe₃N-NMCN

cathode delivers satisfactory electrochemical performance in RT Na–S batteries, in terms of specific capacity (1165.9 mA h g⁻¹ at 167.5 mA g⁻¹), rate capability (658.4 mA h g⁻¹ at 16750 mA g⁻¹), and cycling stability (almost no capacity attenuation after 2800 cycles at 8375 mA g⁻¹). The robust hierarchical cathode design in this work demonstrates effectiveness in developing a stable cathode with high mass loading and stable kinetics, which can be generalized to other batteries systems. A simple graphical sketch of the Na–S cell proposed and the advantages of the S@Fe₃N-NMCN cathode are shown in Fig. 1a, which embodies the underlying reasons for the boosted performance.

Results and discussion

Characterization of Fe₃N-NMCN and S@Fe₃N-NMCN. To obtain a promising reservoir for sulfur (Fe₃N-NMCN), commercialized bacterial celluloses (BC) infiltrated with FeCl₃·6H₂O were carbonized at 300 °C for 1 h and 800 °C for 2 h under a low-pressure NH₃ flow. The purpose of the treatment at the low temperature of 300 °C is to stabilize the structure by evaporating those volatile species in the BC precursor (such as CO, CO₂, methanol, and acetic acid)²⁰, before the final carbonization of BC at a high temperature of 800 °C. XRD and Raman results in Supplementary Fig. 1a–b confirm that the bare BC precursor can be precarbonized at 300 °C and the structure remains almost unchanged at the elevated temperature.

As listed by elemental analysis in Supplementary Table 1, the pristine BC consists of 46.86 wt.% C, 0.12 wt.% N, 46.37 wt.% O and 6.65 wt.% H. The small amount of “intrinsic” nitrogen atoms (0.12 wt.%) come from the residual nitrogen-containing compounds left by the culture media and secretions. When treated at 300 °C, most of the O/H volatilizes and a large amount of N (31.45 wt.%) is doped. As the temperature goes up, the amount of N/O/H reduces while that of C increases remarkably. Finally, the content of C, N, O and H in BC-800 are 89.77 wt.%, 6.45 wt.%, 2.56 wt.% and 1.22 wt.%, respectively.

XPS analyses (Supplementary Figure 1c and Supplementary Table 2) manifest that the amount of O=C species increases while those of O–C and O–C–O decrease dramatically when the temperature is raised. The final BC-800 is characterized by dominant O=C groups which have been reported to boost the affinity between the carbon anode and sodium ions^{21,22}, a favorable feature for performance enhancement. Meanwhile, pyridinic and pyrrolic N are two main N functional groups that can strongly bond to polysulfides and increase electronic conductivity^{23–25}. FESEM images in Supplementary Figure 1d show that these composite fibers become thinner with the increasing temperature. In addition, the FeCl₃·6H₂O turns into Fe₂O₃ under the low-temperature treatment (around 300 °C) and then fully converts into Fe₃N at 800 °C (Supplementary Fig. 2).

The as-obtained Fe₃N-NMCN composite retains the multilayered morphology of the pristine BC (Fig. 1b and Supplementary Fig. 3a–c) and maintains a self-supporting structure (inset of Supplementary Fig. 3a) with a thickness around 350 μm (Supplementary Fig. 3d). Each layer is interconnected by nanosized carbon fibers with a wide diameter distribution around 10–100 nm (Fig. 1c and Supplementary Fig. 3e–f). The TEM images in Fig. 1d and Supplementary Fig. 1g suggest that nanoparticles with a size of 3–10 nm are tightly implanted in these carbon nanofibers. The intertwined self-standing multilayer carbon networks can create a continuous pathway for electrons/ions (the electronic conductivity of carbonized bacterial cellulose aerogel can reach 20.6 S m⁻¹²⁶) and accommodate the volume change of active materials. Plentiful macropores generated by the interconnection of carbon layers (Fig. 1b and Supplementary Fig. 3h–i) can offer more voids to achieve high-sulfur loading.

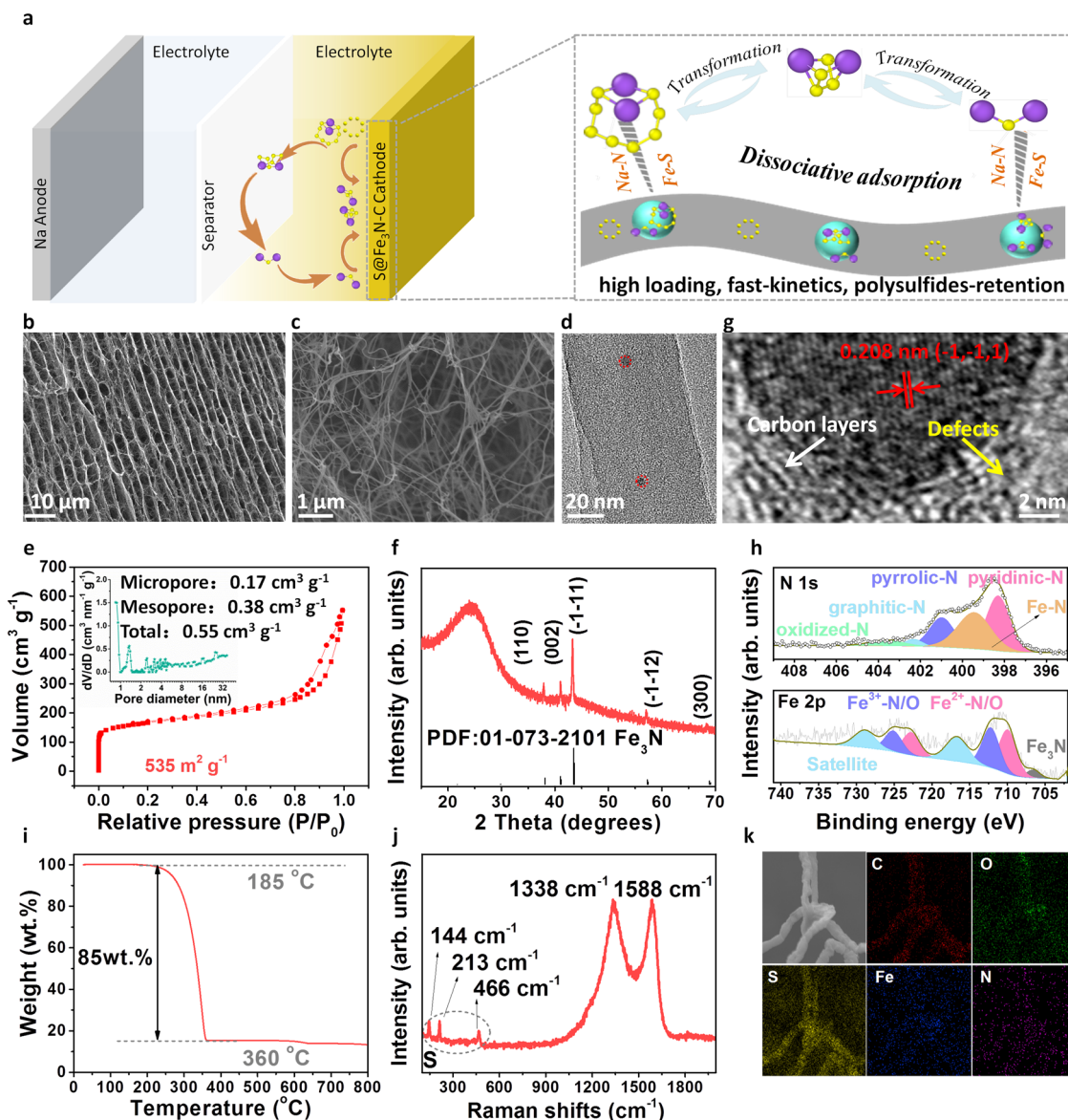


Fig. 1 Characterization of $\text{Fe}_3\text{N-NMCN}$ and $\text{S@Fe}_3\text{N-NMCN}$. **a** Graphical sketch of the current Na-S cell and the function of the $\text{S@Fe}_3\text{N-NMCN}$ cathode. **b-h** SEM (**b-c**), TEM (**d**), adsorption isotherm (**e**), pore-size distribution (inset of **e**), XRD (**f**), HRTEM (**g**), N 1s and Fe 2p spectra (**h**) of $\text{Fe}_3\text{N-NMCN}$. **i-k** TG curve (**i**), Raman spectrum (**j**), and EDS mapping images (**k**) of $\text{S@Fe}_3\text{N-NMCN}$.

Brunauer-Emmert-Teller (BET) analysis and corresponding pore-size distribution were used for a more detailed investigation of the porous structure, as shown in Fig. 1e and Supplementary Fig. 4. The BET surface area, total pore volume, micropores volume, and mesopores volume of the $\text{Fe}_3\text{N-NMCN}$ composite, BC carbonized in Ar (abbreviated as BC-Ar) and BC carbonized in NH_3 (abbreviated as BC- NH_3) are compared in Supplementary Table 3. The BET-specific surface area of the $\text{Fe}_3\text{N-NMCN}$ composite is as high as $535 \text{ m}^2 \text{ g}^{-1}$, much higher than those of BC- NH_3 ($425 \text{ m}^2 \text{ g}^{-1}$) and BC-Ar ($411 \text{ m}^2 \text{ g}^{-1}$), providing prolific space for accommodating vast amount of sulfur. Moreover, the composite possesses a mixture of micropores ($0.17 \text{ cm}^3 \text{ g}^{-1}$), mesopores ($0.38 \text{ cm}^3 \text{ g}^{-1}$), and macropores (inset of Fig. 1e). It has been reported that the synergistic employment of hierarchical pores is an effective strategy to immobilize different types of S species and enable high-sulfur content^{2,27,28}. Micropores are promising reservoirs for accommodating small S molecules and retaining NaPs. However, the limited number of micropores always restricts the elevation of S content. Mesopores/macropores

can help enhance sulfur encapsulation and then realize a high S loading rate. Moreover, mesopores/macropores would greatly accelerate the electron/ion diffusion and offer enough space for the volumetric expansion of sulfur. Hence, the high specific surface area, in conjunction with the hierarchical pore structure, makes the composite a promising high-sulfur-content host.

The phase information of these nanoparticles was firstly investigated by X-ray diffraction (XRD) technique (Fig. 1f). Five characteristic peaks at 37.9° , 41.0° , 43.3° , 57.1° , and 68.7° are ascribed to the (110), (002), (-1-11), (-1-12), and (300) reflections of crystalline Fe_3N (PDF: 01-073-2101) with a hexagonal $P312$ space group²⁹. The distinct lattice fringes with a d-spacing of 0.208 nm displayed by the high-resolution TEM (HRTEM) image (Fig. 1g) conforms to the (-1,-1,1) lattice plane of Fe_3N . The randomly oriented short carbon layers shown in Fig. 1g demonstrate the non-graphitized nature of the as-obtained carbon material. Besides, some defects can be observed mainly due to the N doping^{30,31}, as indicated by the yellow arrow. The disordered structure, together with abundant defects, contributes

favorably to the diffusion of sodium ions as well as the adsorption/catalytic reaction between Fe_3N and NaPSs.

X-ray photo-electron spectroscopy (XPS) (Fig. 1h) is another indication of Fe_3N . In N $1s$ spectrum, a distinct Fe-N peak can be distinguished at 399.5 eV^{32–34}. More importantly, Fe $2p$ spectrum exhibits a peak ascribed to Fe_3N ^{32–34} at the binding energy of 706.9 eV. Peaks at binding energies of 709.4/722.5 and 711.9/724.7 eV are originated from Fe^{2+} -N/O and Fe^{3+} -N/O, due to the surface oxidation of the sample. Peaks at binding energies of 715.8 and 728.9 eV are satellite peaks. The existence of Fe_3N is also supported by the Raman spectrum in Supplementary Figure 5, in which peaks at 211, 280, and 383 cm^{-1} are assigned to Fe_3N according to the previous report³⁵. The amorphous feature of carbon fibers is also revealed by the broad D/G bands at 1339/1591 cm^{-1} . Furthermore, the N $1s$ XPS spectrum verifies the existence of nitrogen-containing functional groups introduced during the NH_3 treatment process, including oxidized-N, graphitic-N, pyrrolic-N, pyridinic-N at binding energies of 403.6, 401.9, 400.7, 398.2 eV, respectively. It is believed that the doped N especially pyridinic and pyrrolic nitrogen can bond strongly to polysulfides and increase electronic conductivity^{23–25}. The content of Fe_3N in the Fe_3N -NMCN composite is 11 wt.%, according to TGA tests (Supplementary Fig. 6). In addition, based on the elemental analysis in Supplementary Table 4, the doped N in Fe_3N -NMCN is calculated to 9.36 wt.%, higher than those in BC- NH_3 (6.45 wt.%) and BC-Ar (0.34 wt.%). The XPS depth profiling results (Supplementary Fig. 7) after 0, 60, 120, 180 s of sputtering further demonstrate that both the N-doping and Fe_3N are distributed uniformly through the whole matrix.

The above results suggest the successful embedding of Fe_3N into N-doped multilayer carbon networks (NMCN), constructing a Fe_3N -NMCN composite as a high-loading host for Na-S batteries. First, the micropores/mesopores in nanofibers and the mesopores/macropores between layers can offer adequate space for sulfur loading, which guarantees the target of high-sulfur content. Second, the electronic conductivity ($0.1\text{--}1.0 \times 10^{-5} \text{ S cm}^{-1}$)³⁶, high ionic diffusion ability ($1.7\text{--}3.6 \times 10^{-13} \text{ cm}^2 \text{ s}^{-1}$)³⁷ and polar surface of Fe_3N nanoparticles would endow the as-proposed cathode excellent reaction kinetics and facilitate the immobilization/transformation of polysulfides. Third, the nano-sized N-doped carbon fibers can offer interconnected conductive networks for the rapid migration of electrons and assist the adsorption/conversion of NaPSs.

Thus, we can load very high-sulfur content up to 85 wt.% (2.6 mg cm^{-2}) into the Fe_3N -NMCN composite (Fig. 1i) through a melting-diffusion method. The sulfur loading allows high specific energy for practical applications, outperforming other studies in which sulfur loadings are below the 50 wt.% range. Moreover, it is believed that further strategies to compress the porous S@ Fe_3N -NMCN cathode can render a close packing of carbon fibers and therefore a thinner electrode, promising for high-energy density (Supplementary Fig. 8). The evident characteristic peaks of S_8 (PDF: 00-024-0733) were observed by XRD (Supplementary Fig. 9), which certifies the successful S deposition and adsorption in the Fe_3N -NMCN composite. The characteristic peaks of carbon (at 1338, 1588 cm^{-1}) and sulfur (at 144, 213, 466 cm^{-1}) were all detected by Raman (Fig. 1j) throughout the composite, verifying the complete and uniform penetration of sulfur through the material. In addition, a sharp decrease of specific surface area ($32 \text{ m}^2 \text{ g}^{-1}$) and pore volume ($0.068 \text{ cm}^3 \text{ g}^{-1}$) of the infiltrated material (Supplementary Fig. 10) suggests that a large proportion of pores are filled with sulfur. The residual pores will serve as an accommodation for the volume expansion during cycles.

FESEM and EDS mapping analyses of S@BC-Ar, S@BC- NH_3 , and S@ Fe_3N -NMCN were provided in Fig. 1k and Supplementary

Fig. 11. It is obvious that all three composites contain uniform distribution of sulfur without forming any bulk particles even under such a high S loading. The mapping images confirm again the uniform distribution of sulfur and also reveal that the self-standing structure is well preserved after S deposition. The above results demonstrate that a large amount of sulfur had been successfully embedded into the as-synthesized composites.

Interaction between NaPSs and Fe_3N -NMCN. The capability of the Fe_3N -NMCN composite to serve as an adsorbent for polysulfides was carefully probed (Fig. 2). Figure 2a compares the adsorption capability of 5 mg Fe_3N -NMCN composite, GO, Super P, BC-Ar, and BC- NH_3 in Na_2S_6 -DOL/Diglyme solution (deep yellow color without any adsorbents). The color of the solution with Super P and BC-Ar remains almost unchanged, which is similar with most of the previous reports^{27,28,38} that used non-polar carbon host materials. In contrast, a moderate adsorption ability to polysulfides is exhibited by BC- NH_3 (comparable to that of GO), as demonstrated by the slight decoloration feature of the solution including BC- NH_3 , which would be resulted from the doping nitrogen (especially the pyridinic and pyrrolic N) in carbon fibers and its high surface area. Notably, the incorporation of Fe_3N dots (the Fe_3N -NMCN composite) enables a significantly rapid color fading in only 10 min, indicating a strong adsorption ability for polysulfides. Density functional theory (DFT) calculations were carried out to elucidate the strong binding interplay between Fe_3N and polysulfides. It is demonstrated that Fe_3N can prompt strong adsorption and fast dissociation of sodium polysulfides. While the Fe_3N dots play a dominant role in the adsorption of polysulfides, the contribution of doping N can not be ignored, as seen in the moderate color fading of the Na_2S_6 -DOL/Diglyme solution (BC- NH_3). Together, the synergistic effect of Fe_3N dots, doped N, and large surface area with abundant pores provides an effective strategy to address the issue of polysulfide shuttling.

UV-Vis spectra further support the above results, as shown in Fig. 2b. The original solution presents two broad bands at 424/612 nm that completely vanish after adsorbed by Fe_3N -NMCN for 24 h. These results prove the adsorption ability of the Fe_3N -NMCN composite to polysulfides, which can suppress the shuttling of polysulfides and ultimately enhance cycling stability. To verify whether the observed change in UV-Vis spectra is caused by adsorption or chemical reaction with precipitation of S-containing species, we analyzed the powders after 24 h of adsorption by XRD, SEM, and EDS. As shown in Supplementary Fig. 12a, the XRD patterns show no other peaks other than the (002) diffraction peak at $\sim 26.0^\circ$ (due to the amorphous carbon) and the peaks corresponding to Fe_3N in Fe_3N -NMCN. This suggests that no new compounds form as a result of chemical reactions. Furthermore, SEM and EDS mapping images in Supplementary Fig. 12b–i demonstrate that there is no aggregation and all elements are uniformly dispersed in these substrates. The above results thus verify that the changes in UV-Vis spectra should be originated from the adsorption of Na_2S_6 .

Furthermore, XPS spectra of the bare Fe_3N -NMCN powder and the Fe_3N -NMCN- Na_2S_6 composite were analyzed to investigate the underlying adsorption principles. An evident Na-N peak emerges at 1074.7 eV (Fig. 2c), besides the signal arisen from polysulfides (1071.7 eV). Concurrently, all peaks in the N $1s$ spectrum (Supplementary Fig. 13) move slightly to higher binding energies, although the shape of the spectrum remains basically unchanged. In addition, polar Fe-S bonds appear in the S $2p$ (159.3/160.5 eV, Fig. 2d) and Fe $2p$ spectrum (714.4/727.2 eV, Fig. 2e), which is helpful for immobilizing polysulfides. The peaks located at 164.1/165.4 eV in S $2p$

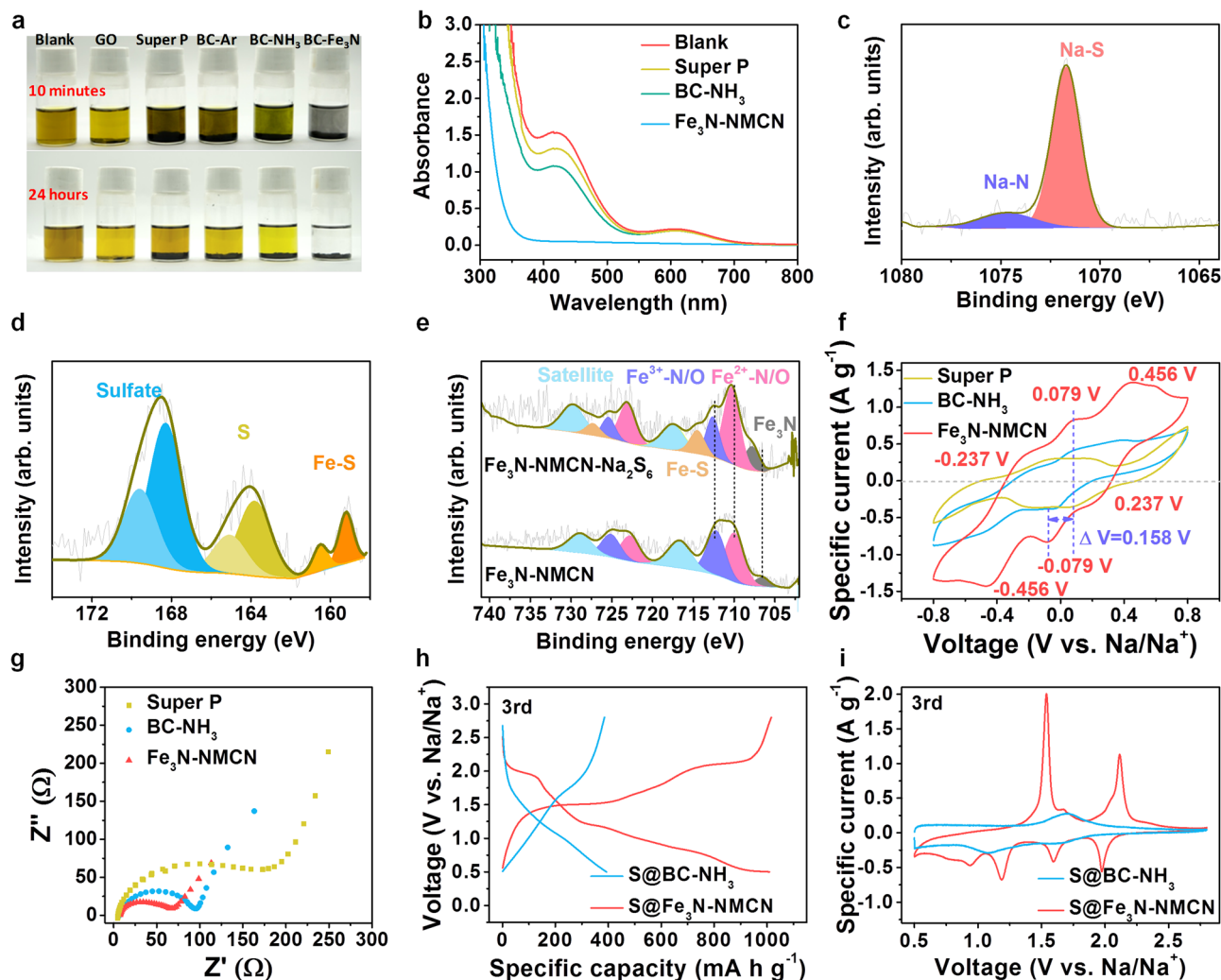


Fig. 2 Interaction between NaPSs and $\text{Fe}_3\text{N-NMCN}$. **a** Optical images of the blank Na_2S_6 solution and solutions with $\text{Fe}_3\text{N-NMCN}$, BC-NH_3 , BC-Ar , GO , and Super P after 10 min and 24 h. **b** UV-Vis spectra of the blank solution and solutions with $\text{Fe}_3\text{N-NMCN}$, BC-NH_3 , and Super P after 24 h. **c**, **d** $\text{Na } 1s$ (**c**) and $\text{S } 2p$ (**d**) XPS spectra after infiltrated with Na_2S_6 . **e** Comparison of $\text{Fe } 2p$ XPS spectra before and after Na_2S_6 adsorption. **f**, **g** CV curves (**f**) and EIS spectra (**g**) of symmetric cells with $\text{Fe}_3\text{N-NMCN}$, BC-NH_3 , and Super P as cathodes. **h**, **i** Comparison of voltage-capacity curves at 167.5 mA g^{-1} (**h**) and CV curves at 0.2 mV s^{-1} (**i**) between $\text{S@Fe}_3\text{N-NMCN}$ and S@BC-NH_3 .

spectrum correspond to S-S bonds, while peaks at $168.4/169.7 \text{ eV}$ are from the oxidized sulfates. Based on the above analyses, the $\text{Fe}_3\text{N-NMCN}$ exhibits both sodiophilic (Na-N bonds) and sulfiphilic (Fe-S bonds) affinity with NaPSs, making it an attractive Na-S host.

To evaluate the catalytic effect of $\text{Fe}_3\text{N-NMCN}$ on polysulfides transformation, cyclic voltammetry (CV) curves of symmetric cells with an electrolyte formed by Na_2S_6 -DOL/Diglyme were gathered (Fig. 2f). The symmetric cells with both BC-NH_3 and Super P exhibit low response currents without any staged peaks. In Metal-S batteries, well-defined redox peaks with small voltage differences signify excellent catalytic activity in the kinetic conversion of polysulfides. However, staged redox peaks in symmetric cells are rarely observed in the Na-S battery literatures¹⁰. In contrast, the CV of $\text{Fe}_3\text{N-NMCN}$ shows evident current response and three pairs of well-defined peaks (at $0.24/-0.24$, $-0.08/0.08$, and $-0.46/0.46 \text{ V}$, respectively). As Na_2S_6 is the only active reactant, the peak located at -0.08 V is assigned to the reduction from Na_2S_6 to short-chain NaPSs while the peak at -0.46 V is originated from the conversion of short-chain NaPSs to Na_2S . Consequently, the peak at 0.24 V corresponds to the

reduction of S_8 to Na_2S_6 . Notably, the polarization of the $\text{Fe}_3\text{N-NMCN}$ electrode (0.16 V) is as small as those reported in the literature for Li-S batteries^{39,40}. Overall, the high current response, well-defined peaks, and small polarization between redox peaks all refer to the strong catalytic ability of the $\text{Fe}_3\text{N-NMCN}$ electrode, which effectively accelerates the electrochemical transformation of NaPSs.

The resistance of the $\text{Fe}_3\text{N-NMCN}$ electrode is low (71Ω for $\text{Fe}_3\text{N-NMCN}$ vs. 95Ω for BC-NH_3 and 185Ω for Super P , Fig. 2g). This figure certifies that the electronic conductivity and interfacial affinity between $\text{Fe}_3\text{N-NMCN}$ and polysulfides are effectively enhanced. This would facilitate the surface diffusion and subsequent conversion of polysulfides. The accelerated dynamics is also reflected by discharge/charge curves of the assembled Na-S cells (Fig. 2h), where the $\text{S@Fe}_3\text{N-NMCN}$ cathode shows smaller polarizations. Correspondingly, more staged plateaus along with larger specific capacities are exhibited by the $\text{S@Fe}_3\text{N-NMCN}$ cathode. Likewise, the CV curves of $\text{S@Fe}_3\text{N-NMCN}$ in Fig. 2i present sharper peak profiles with much larger currents, suggesting the kinetics advantage of $\text{S@Fe}_3\text{N-NMCN}$ for the conversion process.

DFT calculations and AIMD simulations. To gain further insight on the catalytic performance of Fe_3N in Na–S batteries, a theoretical investigation based on DFT calculations^{41–45} was conducted. The (–1–11) plane of Fe_3N was representatively chosen for calculation according to our XRD and TEM observations. The adsorption energy (E_{ad}) was defined as $E_{\text{ad}} = E_{\text{sub+molecule}} - E_{\text{sub}} - E_{\text{molecule}}$, where $E_{\text{sub+molecule}}$, E_{sub} , and E_{molecule} are the total potential energies of the substrate adsorbing a molecule, the substrate and the isolated molecule, respectively. Numerous geometries of Na_2S_n ($n = 1, 2, 4, 6$ and 8) on Fe_3N (–1–11) were investigated and typical configurations were given in Fig. 3a. The calculated adsorption energies of various sodium polysulfides species on the (–1–11) surface of Fe_3N were collected in Fig. 3b. The molecular adsorption energy of Na_2S on Fe_3N centers at -5 eV, manifesting that Fe_3N can strongly anchor Na_2S on its surface, as compared with other samples, such as NiS_2 , metal^{46,47}, Mxene ⁴⁸, MOFs ⁴⁹, and carbon materials^{12,46,47,49,50}. It is also unveiled that the strong polar-polar interaction between NaPSs and Fe_3N results in an obvious dissociation of Na_2S_n molecules. Moreover, Fe_3N is prone to facilitate the dissociation of long-chain polysulfides.

Furthermore, ab initio molecular dynamics (AIMD) simulation was performed to unfold the dissociation process of Na_2S_8 following the adsorption on Fe_3N . Figure 4a–c shows the structure, differential charge density, and potential energy evolution during the dissociative adsorption of Na_2S_8 on Fe_3N (–1–11) as a function of AIMD simulation time. Our AIMD simulation suggests that the dissociative adsorption is dominated by the debonding of S atoms from the molecule and subsequent rebonding to Fe_3N surface, in an incremental fashion. As shown in Fig. 4a–b, as the AIMD simulation proceeds, an increasing number of S atoms, 1S (1.1 ps) \rightarrow 3S (1.74 ps) \rightarrow 4S (3.86 ps) \rightarrow 8S (9.53 ps), debond from the molecule and form new bonds with the Fe_3N substrate. Correspondingly, the total potential energy of the system drops in a series of steps (Fig. 4c). During the dissociation process, charges are transferred to directional regions near an S atom and three nearest Fe atoms, forming new bonds between the S atom and the Fe_3N substrate, in line with the XPS result in Fig. 2c–e. All S atoms from Na_2S_8 have adsorbed on the Fe_3N surface in ~ 9.53 ps and then the Na_2S_8 molecule is completely dissociated with an energy drop of about 20 eV. These findings highlight that the Fe_3N delivers a powerful interaction with NaPSs and can catalyze the dissociation of polysulfides.

Electrochemical energy storage performances of the Na–S@ Fe_3N -NMCN cell. We expect the above S@ Fe_3N -NMCN with well-designed structure and critical functional components to be a desirable positive electrode active material for RT Na–S batteries. The redox behavior was first examined by CV with the voltage range from 2.8 to 0.5 V at a scan rate of 0.2 mV s^{-1} (Fig. 5a). In the first cathodic process, only a broad peak is observed at the voltage range of 1.5–0.8 V, while several well-defined oxidative peaks (at 2.13, 2.01, 1.87, and 1.62 V) emerge in the following charge process. The redox behavior in the following cycles is very different from that in the first cycle, which might be rooted in the decomposition of electrolytes to form solid electrolyte interphase (SEI) and different reaction process due to the electrochemically activation of S/polysulfides⁵¹. As a contrast, the BC-NH₃ was loaded with sulfur and employed as a cathode (S@BC-NH₃) for Na–S batteries (Supplementary Fig. 14). The S@BC-NH₃ cathode delivers different CV curves (Supplementary Fig. 15) with S@ Fe_3N -NMCN. Two broad peaks (1.56, 1.05 V) are observed during the first cathodic process, while a sharp peak at 1.90 V and a broad peak at 1.73 V arise in the following charge process. Besides, the S@BC-NH₃ cathode displays smaller current response and larger polarization. The above results indicate that the S@ Fe_3N -NMCN cathode enables a more kinetically efficient redox reaction process and low intrinsic resistance.

Figure 5b is galvanostatic discharge/charge profiles of the S@ Fe_3N -NMCN cathode at 167.5 mA g^{-1} with an electrolyte/sulfur (E/S) ratio of $18.2 \mu\text{L mg}^{-1}$, where the transition behavior is highly consistent with the CV results. It delivers a discharge capacity of $1270.6 \text{ mA h g}^{-1}$ and a charge capacity of $1165.9 \text{ mA h g}^{-1}$, reaching an initial Coulombic efficiency (ICE) of 92%. Note that the employment of the DOL/DIGLYME electrolyte can enhance the electrochemical performance of Na–S batteries as reported by previous literatures^{52,53} and compared with carbonate-based electrolyte (Supplementary Fig. 16), as ether-based electrolytes always function better with metal anodes and form robust SEI. However, it was also recognized by Cui⁵² that a simple S/C cathode cannot retain good cycling stability in the ether-based electrolyte due to the shuttle of dissolved polysulfides, and by Hassoun⁵³ that ether-based electrolytes mitigate neither the polysulfide dissolution nor the polysulfide shuttle. Therefore, the elaborately designed S@ Fe_3N -NMCN cathode contributes to the performance improvement.

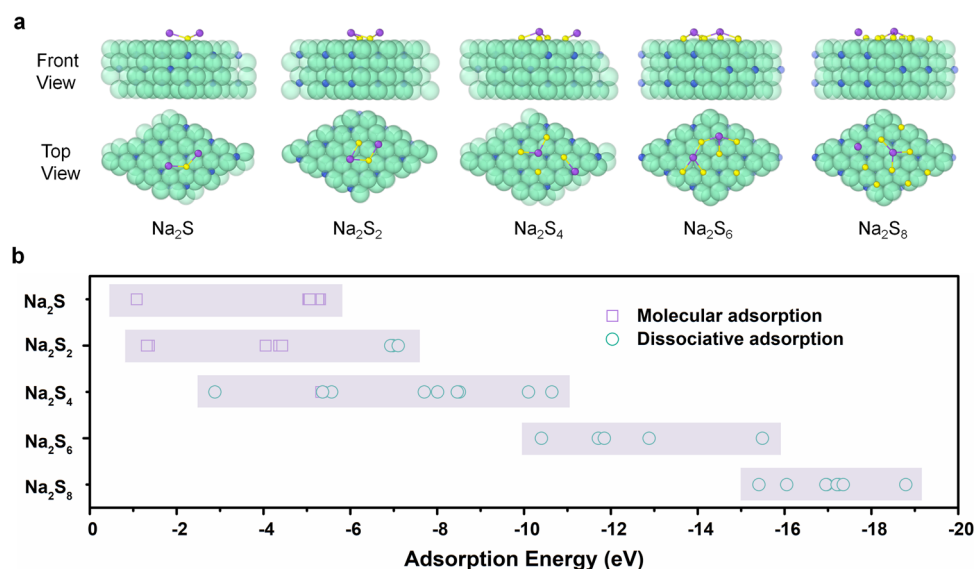


Fig. 3 DFT calculations on the adsorption properties of Fe_3N . **a** Typical adsorption configurations of Na_2S_n ($n = 1, 2, 4, 6$ and 8) on Fe_3N . **b** Calculated adsorption energies of various Na_2S_n ($n = 1, 2, 4, 6$ and 8) on Fe_3N .

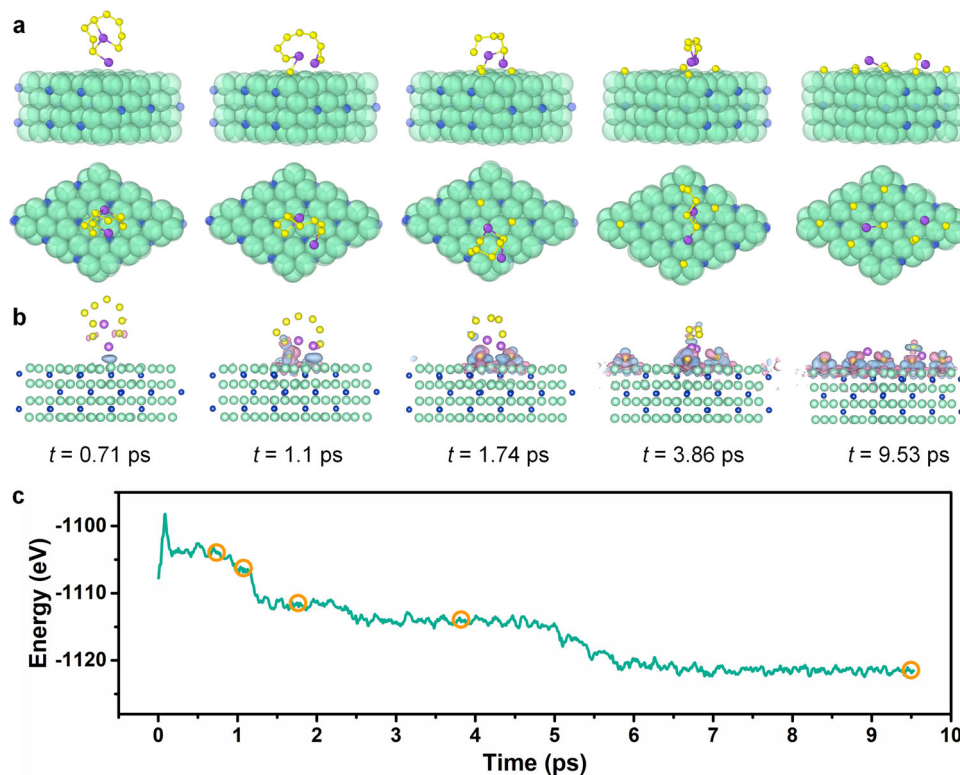


Fig. 4 Theoretical analysis of the Na_2S_8 dissociative adsorption process. Structure (a), differential charge density (b), and potential energy (c) evolution of Na_2S_8 - Fe_3N as a function of AIMD simulation time. Blue/red isosurfaces in (b) represent electron accumulation/depletion regions, respectively. Isosurface scale level is set to $0.02 \text{ e}/\text{\AA}^3$.

Compared with Na-S cells reported in literatures^{7,10-12,27,48,54-61}, the reversible capacity in this work is much closer to the theoretical capacity of sulfur. The capacity contribution from the Fe_3N -NMCN substrate is negligible (only 142 mA h g^{-1} as illustrated in Supplementary Fig. 17a-b). Moreover, the cyclic curve of Fe_3N -NMCN in Supplementary Fig. 17c also demonstrates that the carbon network derived from BC can stabilize the cycle process. By contrast, the S@BC-NH_3 cathode shows smaller reversible capacity ($413.0 \text{ mA h g}^{-1}$) and a low ICE (70%) without well-defined plateaus (Supplementary Fig. 18), demonstrating the crucial role of Fe_3N in improving S utilization rate. On the other hand, the S@BC-NH_3 cathode delivers no overcharge behavior despite of the modest capacity. However, when the S@BC-Ar composite (without N doping in the substrate) was employed as the cathode, a large overcharge capacity is observed (Supplementary Fig. 19), meaning that a severe shuttle of polysulfides has occurred⁶². This confirms that the doped N has a positive influence on bonding sulfur/polysulfides. Similar immobilization of polysulfides by the utilization of heteroatom doping has been widely reported for Li-S and Na-S batteries previously^{23-25,28,54,63,64}. It should be emphasized that even under the identical preparation procedure (mass ratio between S and the substrate, temperature, etc.), smaller amounts of sulfur were immobilized in S@BC-NH_3 (74wt.%) and S@BC-Ar (62wt.%) compared with $\text{S@Fe}_3\text{N-NMCN}$ (85wt.%). These results are well consistent with the BET data in Fig. 2a, where the specific surface area and pore volume of these substrates follow a decreasing order of $\text{Fe}_3\text{N-NMCN}$, BC-NH_3 , and BC-Ar .

Good rate performance was also achieved by the well-designed $\text{S@Fe}_3\text{N-NMCN}$ cathode, as displayed in Fig. 5c and Supplementary Fig. 20. Reversible specific capacities of 1238.6, 1073.7, 936.6, 866.2, 798.6, 706.9, 671.9, 664.2 and $658.4 \text{ mA h g}^{-1}$ are obtained at 167.5, 335, 837.5, 1675, 3350, 8375, 10050, 13400 and 16750 mA g^{-1} , separately. Notably, even at a rather high specific

current of 16750 mA g^{-1} , the reversible capacity retains 53%, among the best rate capability compared with previous reports^{7,10-12,27,48,54-61,65}. What's more, the battery can almost restore to its initial capacity when going back to the low specific current of 167.5 mA g^{-1} . The voltage-capacity profiles (Supplementary Fig. 20) exhibit little hysteresis with increasing specific currents, further confirming the prominent reaction kinetics of as-assembled Na-S cells.

Electrochemical impedance spectroscopy measurements were carried out to investigate the resistance behavior of the sulfur-containing electrodes (Fig. 5d and Supplementary Fig. 21). The corresponding fitting results were listed in Supplementary Tables 5-6. Before cycle, the cell with $\text{S@Fe}_3\text{N-NMCN}$ shows the lowest resistance (67.5Ω) compared to S@BC-NH_3 (93.9Ω) and S@BC-Ar (119.7Ω). In addition, the cell with $\text{S@Fe}_3\text{N-NMCN}$ displays the largest slope at the low frequency Warburg diffusion range, indicating the fastest diffusion of ions in the electrode. After cycled, the cell with $\text{S@Fe}_3\text{N-NMCN}$ also exhibits the lowest SEI impedance (2.03Ω) and charge transfer impedance (1.40Ω). The enhanced performance of $\text{S@Fe}_3\text{N-NMCN}$ compared to their counterparts can be attributed to the improved ionic diffusion and electronic conductivity of Fe_3N .

CV curves at various scan rates of 0.2, 0.5, 0.8, 1, 1.5, and 2 mV s^{-1} were recorded (Supplementary Fig. 22) to investigate the reaction kinetics of the $\text{S@Fe}_3\text{N-NMCN}$ cathode. The peak separation between each pair of redox peaks rises slightly with increasing scan rates (Supplementary Fig. 22a). Slopes calculated from plots of peak currents and square roots of scan rates (Supplementary Fig. 22b) are 393.2, 319.0, 324.5, -272.1 , and -355.0 for A1, A2, A3, C1, and C2, respectively. In contrast, the S@BC-NH_3 cathode reveals inadequate performance at high specific currents (389.6 , 363.0 , 351.7 , 329.8 , 307.9 , 295.7 , 286.7 ,

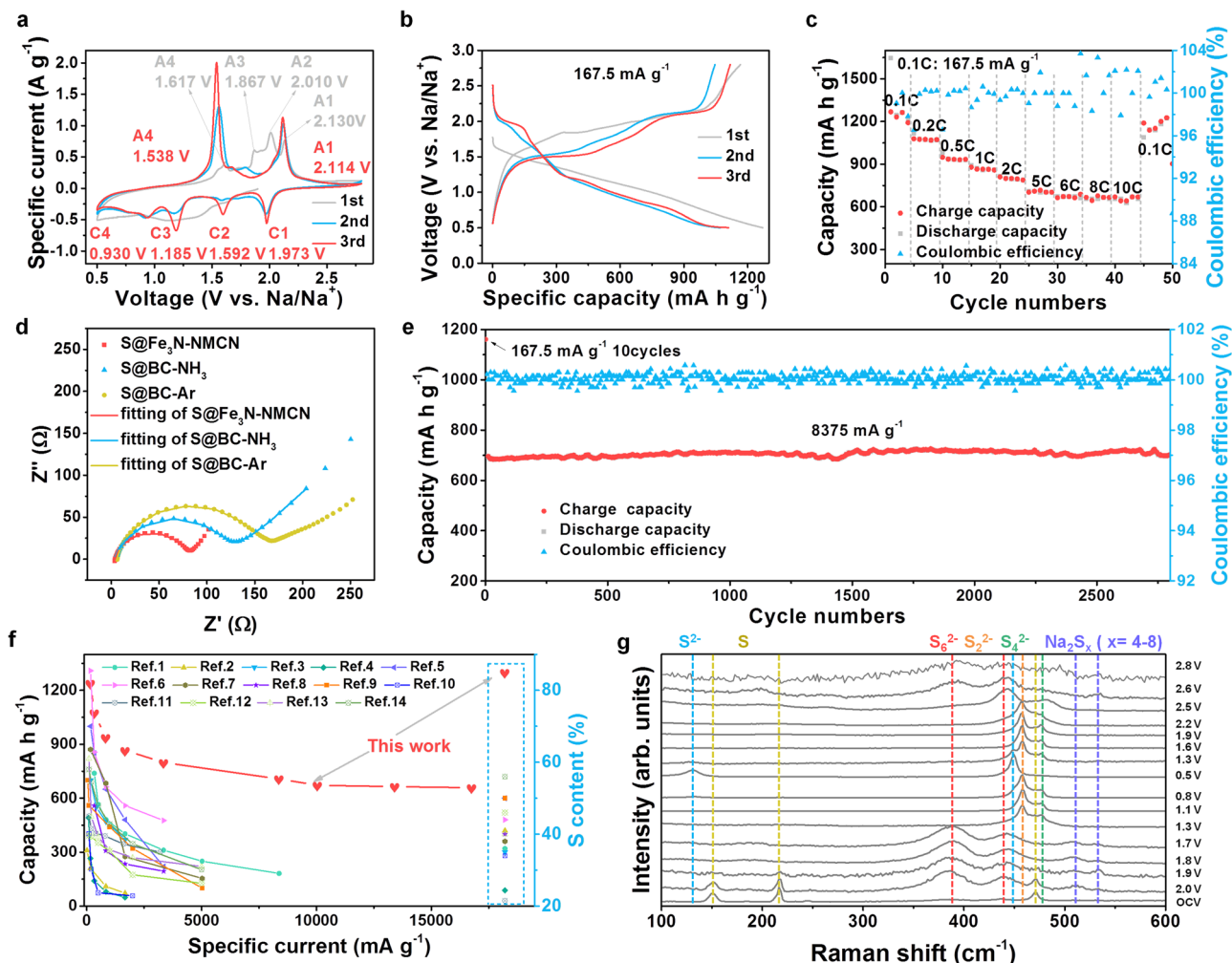


Fig. 5 Electrochemical energy storage performances of the Na-S@Fe₃N-NMCN cell. **a** First three CV curves at a scan rate of 0.2 mV s⁻¹. **b** First three voltage-capacity curves at a specific current of 167.5 mA g⁻¹. **c** Rate capability at specific currents of 167.5, 335, 837.5, 1675, 3350, 8375, 10050, 13400, 16750 mA g⁻¹. **d** Comparison of EIS spectra between BC-Ar, BC-NH₃, and Fe₃N-NMCN before the rate test. **e** Long-term cycling performance at a specific current of 8375 mA g⁻¹. **f** Comparison of electrochemical performance and sulfur content with previous literature. **g** In situ Raman spectra at a specific current of 167.5 mA g⁻¹.

281.7, and 294.1 mA h g⁻¹ at 167.5, 335, 837.5, 1675, 3350, 8375, 10050, 13400, and 16750 mA g⁻¹, respectively (Supplementary Fig. 23). Accordingly, the CV curves exhibit larger voltage hysteresis as the increase of scan rates (Supplementary Fig. 24a). Slopes from plots of peak currents and square roots of scan rates are much smaller (35.0 for A2 and -82.3 for C2 respectively, Supplementary Fig. 24b). As the diffusion coefficient is in direct proportion to the square of slope based on the Randles-Sevcik equation ($I = 2.69 \times 10^5 n^{1.5} A D^{0.5} \nu^{0.5} C$)^{66,67}, it is explicit that the S@Fe₃N-NMCN cathode possesses larger diffusion coefficients. The rate capability of the S@Fe₃N-NMCN electrode is promoted by the strong catalytic ability of Fe₃N as well as the long-range conductive networks formed by N-doped carbon nanofibers and Fe₃N quantum dots.

Another appealing property of the S@Fe₃N-NMCN cathode is the long-term cyclic stability. As illustrated in Fig. 5e and Supplementary Fig. 25, after cycled at 167.5 mA g⁻¹ for ten cycles, the reversible capacity at a rather high specific current of 8375 mA g⁻¹ can reach 696 mA h g⁻¹ and remain almost unchanged after 2800 cycles (698.7 mA h g⁻¹), far better than reported results^{7,10-12,27,48,54-61,65}. Moreover, the battery can achieve a high and steady Coulombic efficiency of around 100%. The slight capacity variation can be due to the electrochemical

activation process (Supplementary Fig. 26 and Supplementary Table 7) and the ambient temperature change^{68,69}. The cycling performance is achieved by the stable structure, good electrical conductivity and strong chemical interaction with NaPSs. From the comparison of the electrochemical performance with that of the current state-of-art Na-S batteries (Supplementary Table 8 and Fig. 5f)^{7,10-12,27,48,54-61,65}, the results obtained in this work are among the best performance reported, in terms of sulfur content, specific capacity, rate capability and cycling stability.

In situ Raman spectroscopy measurements (Fig. 5g and Supplementary Fig. 27) were performed to clarify the reaction process of the S@Fe₃N-NMCN cathode. Characteristic peaks of S₈⁷⁰ emerge at 151, 217, and 471 cm⁻¹ when the battery is in open-circuit voltage (OCV), and become weak after discharging to 2.0 V. Accompanied by the dissolution of S₈, a series of long-chain NaPSs appear at 390, 442, 508 and 534 cm⁻¹. Afterwards, at 1.3 V, two new peaks ascribed to Na₂S₄⁵⁰ and Na₂S₂⁵⁰ arise at ~478 and 458 cm⁻¹ respectively. Peaks of Na₂S⁷¹ (at 131 and 449 cm⁻¹) emerge at 0.8 V and the intensity increases gradually until fully discharged to 0.5 V. In the following charge process, these peaks change oppositely from Na₂S to Na₂S₄, Na₂S₆, Na₂S_x (x = 4-8); however, no signals of S₈ are discovered, in agreement with previous reports^{72,73}. Different from previous reports that

peaks of S_8 exist throughout the whole discharge/charge process¹⁰ and the deposited Na_2S can still be detected in the full-charged electrode⁷¹, a highly reversible reaction between Na_2S_8 and Na_2S_2 is presented in the as-proposed $S@Fe_3N$ -NMCN cathode. In a whole, the discharge/charge process correlates to two distinct transitions from Na_2S_8 to Na_2S_x ($x = 4-8$) in 2.8–1.3 V and then to Na_2S in 1.3–0.5 V. As for the CV curves, the C1/C2 peaks may correspond to the conversion of long-chain NaPSs into short-chain, while the C3/C4 peaks may relate to the transformation of short-chain NaPSs to Na_2S .

We also carried out post-mortem analyses for the separators, the Na metal electrodes, and the as-employed electrodes disassembled from cells with $S@BC$ -Ar, $S@BC$ - NH_3 , and $S@Fe_3N$ -NMCN, respectively (Supplementary Figs. 28–33). Generally, the dissolution and shuttle of polysulfides lead to more yellowish separators. As can be seen, in contrast to the most yellowish separator from $S@BC$ -Ar, the separator from $S@BC$ - NH_3 shows less yellowish and no visible yellow color can be observed in the separator from $S@Fe_3N$ -NMCN, suggesting increasingly inhibited dissolution and shuttle of polysulfides. For the cycled Na electrodes, dendrites are barely found in case of $S@Fe_3N$ -NMCN when compared to their counterparts. In addition, a loose layer is formed on the cycled Na anode from BC -Ar, while the surface with $S@Fe_3N$ -NMCN is smooth and clean. It has been reported⁷⁴ that a synergistic effect of lithium polysulfide and lithium nitrate in ether-based electrolyte can lead to a stable and uniform SEI layer on Li metal. However, it was also recognized that polysulfides alone cannot prevent the dendrite growth and minimize the electrolyte decomposition. In view of this, a better surface morphology of the Na anode for $S@Fe_3N$ -NMCN compared with $S@BC$ -Ar is resulted from the less shuttling of polysulfides to the Na anode as only polysulfides are presented in the electrolyte and no synergistic effect can be generated. The bonding ability to polysulfides achieved by Fe_3N , nitrogen doping, large surface area, and cathode porosity, can restrain the dissolved polysulfides in the cathode area. Thus, little polysulfides can enter into the anode area and deteriorate the Na anode. Supplementary Figs. 30–33 show that all three cycled electrodes can maintain the original morphology and all elements are uniformly distributed without aggregation; however, the $S@BC$ -Ar electrode shows a smoother surface indicating the dissolution of some active sulfur materials into the electrolyte. The above results thus suggest that the dissolution and shuttle of polysulfides can be largely inhibited by Fe_3N -NMCN.

To further check the effect of electrolyte volume and the utilization of sulfur in Na–S batteries, we first studied the performance of the $S@Fe_3N$ -NMCN electrode at different E/S ratios. As displayed in Supplementary Fig. 34a–b, in an E/S ratio range from 10.9:1 to 18.2:1, the capacities obtained in Na–S batteries are higher than most of the recently published literatures on Li–S batteries^{13,14,69,75} and Na–S batteries⁵⁰. In addition, the $S@Fe_3N$ -NMCN electrode can still reach an acceptable capacity of $810.5 \text{ mA h g}^{-1}$ at a very low E/S ratio of $7.27 \mu\text{L mg}^{-1}$. The capacity fading at low E/S ratios can be explained by the Na–S reaction mechanism that the electrochemical process is assisted by the dissolution of polysulfides and the fact that the increase of polysulfides concentration at low E/S ratios would result in the expansion of battery resistance.

Next, we studied the reaction process of the Na–S battery at a low E/S ratio of $7.27 \mu\text{L mg}^{-1}$ by in situ XRD and ex situ XPS, as shown in Supplementary Fig. 35. Supplementary Fig. 35a–b demonstrate that the sulfur converts to Na_2S_2 when the discharge voltage drops to around 1.6 V. In the following charge process, the Na_2S_2 can be completely converted to Na_2S_8 again. Ex situ XPS spectra in Supplementary Fig. 35c–e lend further support to

the in situ XRD results. The original electrode shows a pair of peaks ascribed to sulfur at binding energies of 163.9/165.0 eV. When discharged to 0.5 V, two strong peaks of S_2^{2-}/S^{2-} appear at 162.1 and 163.2 eV. The above results show that a series of highly reversible reactions between Na_2S_8 and Na_2S_2 can be achieved even at such a low E/S ratio of $7.27 \mu\text{L mg}^{-1}$, demonstrating the potential of $S@Fe_3N$ -NMCN to serve as a high-performance electrode for Na–S batteries.

It is worth mentioning that the proposed Fe_3N -NMCN substrate can also be applied to other multi-electron redox materials. For example, when 77% Se is incorporated ($Se@Fe_3N$ -NMCN, Supplementary Fig. 36a), an average specific capacity of $671.4 \text{ mA h g}^{-1}$ is obtained at 70 mA g^{-1} and can maintain 74% at 7000 mA g^{-1} ($496.4 \text{ mA h g}^{-1}$, Supplementary Fig. 36b–e). In addition, the $S@Fe_3N$ -NMCN electrode is also applicable for Li–S batteries (Supplementary Fig. 37). In an electrolyte of 1 M LiTFSI in DOL/DME (1:1 by volume) with 0.1 M $LiNO_3$, the $S@Fe_3N$ -NMCN electrode can deliver a high reversible capacity of $1345.7 \text{ mA h g}^{-1}$ with an ICE of 94.3% at 167.5 mA g^{-1} (Supplementary Fig. 37a).

The good C-rate and long-cycle performance can be attributed to the synergistic effect of the N-doped carbon nanofibers and Fe_3N quantum dots. The carbon matrix generated from the carbonization of BC in NH_3 possesses several merits, such as large specific surface area, hierarchical pore, N doping, and good electronic conductivity. It can provide enough space to accommodate massive sulfur and adapt the volume change during cycling. The difference of electrostatic charges between the N-doped carbon matrix and polysulfides will also assist the entrapment of NaPSs to prevent shuttling. Furthermore, the electronic conductivity and ion diffusion of Fe_3N quantum dots improve the electrons/ions kinetics, while Fe/N atoms can form strong polar interaction with NaPSs and adsorb/catalyze NaPSs conversion. Besides, other alternative strategies such as the anode protection^{74,76} and the electrolyte/separator modification^{77,78} can be combined to further mitigate the detrimental effects of dissolved Na_2S_x , enabling a better performance and making the as-proposed electrode more practical.

In summary, Fe_3N quantum dots on N-doped multilayer carbon networks (Fe_3N -NMCN) were developed as an electrocatalyst targeting high-loading, fast-kinetics, and polysulfides-retention Na–S batteries. The N-doped multilayer carbon networks featured with large specific areas and hierarchical pores ensure the high-sulfur implementation. The N-doped substrate also provides the necessary physical adsorption due to the porous structure and extra chemical adsorption sites from the N doping. Meanwhile, the sulfur agglomeration and volume expansion are well suppressed by the multilayered carbon networks. In addition to the preceding advantages, the most substantial merit of this structure is the loaded Fe_3N quantum dots, which show strong affinity to polysulfides via Na–N and Fe–S bonds. The engineered multilayered carbon networks loaded with Fe_3N quantum dots efficiently inhibit NaPSs shuttling and promote NaPSs catalyzed reaction. These features of the as-proposed cathode offer high reversible capacity ($1165.9 \text{ mA h g}^{-1}$ at 167.5 mA g^{-1}), excellent rate capability ($658.4 \text{ mA h g}^{-1}$ at 16750 mA g^{-1}), and stable cycling performance up to 2800 cycles, even at a practically relevant sulfur loading of 85wt.%. Most noteworthy, the cathode can be used as a self-standing electrode and the Fe_3N -NMCN host can also be extended to other multi-electron redox materials. This work not only clarifies the underlying mechanism for the improved performance, but also offers a strategy to design high-performance Na–S batteries. In addition to Fe_3N as identified in this work, we expect that many other nitrides can be explored as catalyst materials for Na–S batteries.

Methods

Preparation of Fe₃N-NMCM, BC-NH₃, and BC-Ar. The commercial BC pellicles were first immersed into ethanol and deionized water for ultrasonic and then frozen in liquid nitrogen. In a typical synthesis of Fe₃N-NMCM, a piece of freeze-dried bacterial cellulose with a diameter of 19 mm was infiltrated by 50 μ L ethanol solution of 25 mg mL⁻¹ FeCl₃·6H₂O. After drying at room temperature, these pieces were carbonized at 300 °C for 1 h and then 800 °C for 2 h under a low pressure of NH₃. The heating rate was 5 °C min⁻¹. A low temperature of 300 °C for 1 h was first employed to stabilize the BC structure and then finally carbonized at 800 °C for 2 h. After natural cooling to room temperature, the Fe₃N-NMCM film with a thickness of around 350 μ m was obtained. BC-NH₃ and BC-Ar were obtained by the direct pyrolysis of BC under NH₃ and Ar atmosphere with the same temperature procedure as that of Fe₃N-NMCM. No purification step was employed after the pyrolysis in the synthesis of Fe₃N-NMCM, BC-NH₃, and BC-Ar. The weight of the Fe₃N-NMCM substrate was around 1 mg, while those of BC-Ar and BC-NH₃ were about 0.85 mg.

Preparation of S@Fe₃N-NMCM, S@BC-NH₃, and S@BC-Ar. 10 mg mL⁻¹ carbon disulfide solution of sublimed sulfur was dropwise added into Fe₃N-NMCM, BC-NH₃, and BC-Ar. The mass ratio of sulfur to the composite was kept at 10:1. After the volatilization of carbon disulfide in copper foil-wrapped crucibles at room temperature, it was heated to 155 °C with a temperature ramp of 2 °C min⁻¹ and kept at 155 °C for 12 h to ensure the well permeation of sulfur. After that, the temperature was elevated to 200 °C with a temperature ramp of 2 °C min⁻¹ and maintained at 200 °C for 30 min. Then, S@Fe₃N-NMCM, S@BC-NH₃ and S@BC-Ar were collected after cooling to room temperature. The weight of S@Fe₃N-NMCM was around 6.5 mg. The sulfur in the S@Fe₃N-NMCM electrode was around 5.5 mg. The diameter of S@Fe₃N-NMCM was around 16 mm. The mass loading of S in S@Fe₃N-NMCM was ~2.6 mg cm⁻². The electrolyte/sulfur (E/S) ratio for S@Fe₃N-NMCM was 18.2 μ L mg⁻¹. The thickness of the S@Fe₃N-NMCM electrode was around 300 μ m (Supplementary Fig. 38). To enhance the energy density of the electrode, an effective calendaring-infiltration process can be used to achieve a more compact electrode (Supplementary Fig. 8). The weight of S@BC-NH₃ and S@BC-Ar were around 3.2 and 2.3 mg. The sulfur in S@BC-NH₃ and S@BC-Ar were around 2.35 and 1.45 mg. The electrolyte/sulfur (E/S) ratio for S@BC-NH₃ and S@BC-Ar were 42.6 and 69.0 μ L mg⁻¹.

Adsorption experiment. The Na₂S₆ solution (0.1 mol L⁻¹) was prepared by mixing sodium sulfide (Na₂S) and sulfur with a molar ratio of 1:5 in 1,3-dioxolane (DOL) and Diethylene glycol dimethyl ether (DIGLYME) (1: 1 Vol.%). Then, the solution was sealed with inert gas and stirred at room temperature for 20 h. 5 mg Fe₃N-NMCM, BC-NH₃, BC-Ar, GO and super P were added into the diluted Na₂S₆ solution, respectively, with the blank Na₂S₆ solution as a reference.

Material characterization. The morphologies of these samples were investigated by field-emission scanning microscope (FESEM, JSM-7800F, Japan) and transmission electron microscopy (TEM, JEM-2100, Japan). The EDS spectroscopy attached to FESEM was employed to record the elemental distribution. X-ray diffraction (XRD, Bruker, Advance D8A A25) was employed to investigate the phase information of the as-synthesized products. X-ray photoelectron spectroscopy (XPS) measurements were carried out on a Thermo Scientific ESCALAB 250Xi electron spectrometer. The sulfur contents in the as-prepared composites were determined by a Thermogravimetric analyzer (TGA, Q50, USA). The analyses for the specific surface area and the pore-size distribution were performed on micromeritics ASAP2020 equipped with V4.02 software under N₂ atmosphere. The Non-Local Density Functional Theory (NLDFT) model was used to calculate the dV/dD vs. pore diameter curve. The pretreatment process was applied at 120 °C for 24 h. In addition, ex situ Raman was recorded by Lab-RAM HR Evolution Raman microscope with a 532 nm laser. The power of the 532 nm laser is 50 mW. The acquisition time per spectra is 24 s. The in situ Raman cell was purchased from EL-CELL company. The discharge/charge process of the in situ Raman was performed by a CV program on CHI760E. The corresponding CV curve was shown in Supplementary Fig. 27. Elemental analysis is conducted on Thermo Fisher (Flashsmart).

Ex situ characterizations of the Na₂S₆ infiltrated material after the adsorption test, the cycled electrodes and the cycled Na metals were conducted according to the following steps. Firstly, these materials were filtrated, dried, and collected in the Ar glove box. Then, these materials were pasted on the platform and sealed with a plastic centrifuge tube. Thirdly, the platform was transferred into the chamber of the instrument and vacuumed quickly. Similarly, the XRD platform was sealed by a CAPTON tape.

Electrochemical measurement. To investigate the electrochemical energy storage performances, the S@Fe₃N-NMCM, S@BC-NH₃, and S@BC-Ar composites were directly used as cathodes to assemble coin-type (CR2032) cells in an argon-filled glove box (water and oxygen content lower than 5 ppm) with a calendaring pressure of 50 kg cm⁻². Glass fibers (Whatman, GF1823-110) and sodium foils (Sinopharm Chemical Reagent Co., Ltd., 99.8%) were used as separators and the counter electrodes. The sodium foil was prepared manually during the battery

assembly. The thickness of sodium foils is around 600 μ m (Supplementary Fig. 39). 1 M NaPF₆ dissolved in 4-methyl-1,3-dioxo-cyclopentane/Diglyme (DOL/DIGLYME) (1:1 vol%) was employed as the electrolyte, whereas the water amount in the electrolyte is below 5 ppm. The amount of electrolyte added in each coin-type (CR2032) cell was 100 μ L (an E/S ratio of 18.2 μ L mg⁻¹). In addition, different amounts of electrolytes (80, 60, and 40 μ L, different E/S ratios of 14.5, 10.9, and 7.27 μ L mg⁻¹) were employed to further check the effect of electrolyte volume in Na-S cells. The in situ XRD was conducted under a low E/S ratio of 7.27 μ L mg⁻¹ and thus the corresponding capacity of the in situ cell is 731.5 mA h g⁻¹, which is lower than that reported in the main text (1165.9 mA h g⁻¹ under an E/S ratio of 18.2 μ L mg⁻¹). The in situ cell was purchased from Bruker (Beijing) Technology Co., LTD. A Be foil was used to seal the cell. The in situ XRD was conducted at a specific current of 167.5 mA g⁻¹ and an electrochemical window of 2.8–0.5 V on X-ray diffraction (XRD, Bruker, Advance D8A A25). Each XRD spectrum was collected within 12 min.

All the galvanostatic measurements were conducted on Land BT2000 battery test systems (Wuhan, China) in a voltage range of 2.8–0.5 V under room temperature (25 °C \pm 5 °C) without any climatic/environmental chamber. CV test was carried out on CHI760E electrochemical workstation at scan rates of 0.2, 0.5, 0.8, 1, 1.5, and 2 mV s⁻¹. Zanner electrochemical workstation was used to collect the electrochemical impedance spectroscopy (EIS) measurements in a frequency range of 1 mHz–1 MHz (100 points per spectrum) with an amplitude of 5 mV. The correlation between the peak currents and the square roots of scan rates was determined by the Randles-Sevcik equation: $i_p = (2.69 \times 10^5) n^{1.5} A D^{0.5} C v^{0.5}$, where i_p is the current at an electrochemical reaction, n is the number of electrons participating in one mole of the reaction, A is the electrode-electrolyte interface area (approximately to be the electrode area), D is the apparent diffusion coefficient, C is the mole concentration of Na⁺ in the electrode, and v is the scan rate.

First-principles calculation/simulation. All ab initio calculations were carried out using the Vienna Ab initio simulation package (VASP). Electronic exchange-correlation functional was described by the generalized gradient approximation (GGA) in the form of Perdew-Burke-Ernzerhof (PBE). Core electrons were modeled with projector-augmented wave (PAW) pseudo-potentials (versions of Fe, N, S, and Na_pv as supplied in the VASP package) and a planewave energy cutoff of 520 eV was chosen. A k-point grid of 2 \times 2 \times 1 was used for the adsorption energy calculations and differential charge density analyses, while Γ point only sampling was performed for all molecular dynamics simulations (MD). Gaussian smearing with a width of 0.05 eV was used for the partial occupancies of states. All calculations are spin polarized. A slab configuration of Fe₃N in hexagonal crystal structure was used in all calculations. A vacuum space with thickness $\geq 10 \text{ \AA}$ (depending on molecule positions) was inserted to model-free surface (close-packed plane in our case). The slab configuration contains 108 Fe atoms and 27 N atoms, with the bottom 2 layers fixed (in zero K adsorption energy calculations) or restricted to in-plane motion only (in 300 K ab initio MD simulations). Unrelaxed initial configurations for Na₂S_x ($x = 2, 4, 6, 8$) molecules were adopted from references. The initial adsorption configurations, with all molecule identities preserved by elastic constraints on bonds, were searched by the constrained minima hopping algorithm as implemented in the ASE package. Then molecules and surface atoms are fully relaxed to capture both molecular adsorption and dissociative adsorption processes. Ab initio MD simulations were carried out at 300 K under the NVT (Nose-Hoover thermostat) ensemble. A time step of 1 fs was used for integrating the equation of motion. Visualization and differential charge density analyses were carried out using the Ovito package.

Reporting summary. Further information on research design is available in the Nature Research Reporting Summary linked to this article.

Data availability

The data generated in this study are provided in the Supplementary information and main text.

Code availability

This study does not use any custom code or mathematical algorithm, and code availability is not a mandatory requirement for this work.

Received: 18 March 2021; Accepted: 12 October 2021;

Published online: 03 November 2021

References

1. Park, C.-W., Ahn, J.-H., Ryu, H.-S., Kim, K.-W. & Ahn, H.-J. Room-temperature solid-state sodium/sulfur battery. *Electrochem. Solid-State Lett.* **9**, A123–A125 (2006).

- Xin, S., Yin, Y. X., Guo, Y. G. & Wan, L. J. A high-energy room-temperature sodium-sulfur battery. *Adv. Mater.* **26**, 1261–1265 (2014).
- Manthiram, A. & Yu, X. Ambient temperature sodium-sulfur batteries. *Small* **11**, 2108–2114 (2015).
- Wang, Q. et al. Direct observation of sulfur radicals as reaction media in lithium sulfur batteries. *J. Electrochem. Soc.* **162**, A474–A478 (2015).
- Xiao, J. et al. Following the transient reactions in lithium-sulfur batteries using an in situ nuclear magnetic resonance technique. *Nano Lett.* **15**, 3309–3316 (2015).
- Yu, X. & Manthiram, A. Sodium-sulfur batteries with a polymer-coated NASICON-type sodium-ion solid electrolyte. *Matter* **1**, 439–451 (2019).
- Carter, R. et al. A sugar-derived room-temperature sodium sulfur battery with long term cycling stability. *Nano Lett.* **17**, 1863–1869 (2017).
- Xin, S. et al. Smaller sulfur molecules promise better lithium-sulfur batteries. *J. Am. Chem. Soc.* **134**, 18510–18513 (2012).
- Li, X. et al. Electrospinning-based strategies for battery materials. *Adv. Energy Mater.* **11**, 2000845 (2020).
- Guo, B. et al. Nickel hollow spheres concatenated by nitrogen-doped carbon fibers for enhancing electrochemical kinetics of sodium-sulfur batteries. *Adv. Sci.* **7**, 1902617 (2020).
- Zheng, S. et al. Nano-copper-assisted immobilization of sulfur in high-surface-area mesoporous carbon cathodes for room temperature Na-S batteries. *Adv. Energy Mater.* **4**, 1400226 (2014).
- Yan, Z. et al. Nickel sulfide nanocrystals on nitrogen-doped porous carbon nanotubes with high-efficiency electrocatalysis for room-temperature sodium-sulfur batteries. *Nat. Commun.* **10**, 4793 (2019).
- Cui, Z., Zu, C., Zhou, W., Manthiram, A. & Goodenough, J. B. Mesoporous titanium nitride-enabled highly stable lithium-sulfur batteries. *Adv. Mater.* **28**, 6926–6931 (2016).
- Song, Y. et al. Synchronous immobilization and conversion of polysulfides on a VO₂-VN binary host targeting high sulfur load Li-S batteries. *Energy Environ. Sci.* **11**, 2620–2630 (2018).
- Wu, H. et al. Cobalt nitride nanoparticle coated hollow carbon spheres with nitrogen vacancies as an electrocatalyst for lithium-sulfur batteries. *J. Mater. Chem. A* **8**, 14498–14505 (2020).
- Seh, Z. W., Sun, Y., Zhang, Q. & Cui, Y. Designing high-energy lithium-sulfur batteries. *Chem. Soc. Rev.* **45**, 5605–5634 (2016).
- Xue, W. et al. Intercalation-conversion hybrid cathodes enabling Li-S full-cell architectures with jointly superior gravimetric and volumetric energy densities. *Nat. Energy* **4**, 374–382 (2019).
- Lv, D. et al. High energy density lithium-sulfur batteries: challenges of thick sulfur cathodes. *Adv. Energy Mater.* <https://doi.org/10.1002/aenm.201402290> (2015).
- Bhargava, A., He, J., Gupta, A. & Manthiram, A. Lithium-sulfur batteries: attaining the critical metrics. *Joule* **4**, 285–291 (2020).
- Liang, H.-W. et al. Highly conductive and stretchable conductors fabricated from bacterial cellulose. *NPG Asia Mater.* **4**, e19–e19 (2012).
- Qi, Y. et al. Retarding graphitization of soft carbon precursor: from fusion-state to solid-state carbonization. *Energy Storage Mater.* **26**, 577–584 (2020).
- Qi, Y. et al. Slope-dominated carbon anode with high specific capacity and superior rate capability for high safety Na-ion batteries. *Angew. Chem., Int. Ed.* **58**, 4361–4365 (2019).
- Yu, Q. et al. In situ formation of copper-based hosts embedded within 3D N-doped hierarchically porous carbon networks for ultralong cycle lithium-sulfur batteries. *Adv. Funct. Mater.* **28**, 1804520 (2018).
- Liu, Y. et al. Nitrogen doping improves the immobilization and catalytic effects of Co₉S₈ in Li-S Batteries. *Adv. Funct. Mater.* **30**, 2002462 (2020).
- Shan, Z. et al. Spontaneously rooting carbon nanotube incorporated N-doped carbon nanofibers as efficient sulfur host toward high performance lithium-sulfur batteries. *Appl. Surf. Sci.* **539**, 148209 (2021).
- Wu, Z. Y., Li, C., Liang, H. W., Chen, J. F. & Yu, S. H. Ultralight, flexible, and fire-resistant carbon nanofiber aerogels from bacterial cellulose. *Angew. Chem., Int. Ed.* **52**, 2925–2929 (2013).
- Wang, Y. X. et al. Achieving high-performance room-temperature sodium-sulfur batteries with S@interconnected mesoporous carbon hollow nanospheres. *J. Am. Chem. Soc.* **138**, 16576–16579 (2016).
- Xia, G. et al. Carbon hollow nanobubbles on porous carbon nanofibers: an ideal host for high-performance sodium-sulfur batteries and hydrogen storage. *Energy Storage Mater.* **14**, 314–323 (2018).
- Serghiou, G. et al. Synthesis and high-resolution study distinguishing between very similar interstitial iron nitride structures. *High. Press. Res.* **35**, 28–36 (2015).
- Chen, Y. et al. Nitrogen-doped carbon for sodium-ion battery anode by self-etching and graphitization of bimetallic MOF-based composite. *Chem* **3**, 152–163 (2017).
- Chen, Y. et al. Li metal deposition and stripping in a solid-state battery via Coble creep. *Nature* **578**, 251–255 (2020).
- Soto, G., Cruz, W. de la & Farias, M. H. XPS, AES, and EELS characterization of nitrogen-containing thin film. *J. Electron Spectrosc. Relat. Phenom.* **135**, 27–39 (2004).
- Ren, W. et al. Isolated diatomic Ni-Fe metal-nitrogen sites for synergistic electroreduction of CO₂. *Angew. Chem., Int. Ed.* **58**, 6972–6976 (2019).
- Ma, X. et al. Melamine-assisted synthesis of Fe₃N featuring highly reversible crystalline-phase transformation for ultrastable sodium ion storage. *J. Mater. Chem. A* **8**, 6768–6775 (2020).
- Li, Z., Fang, Y., Zhang, J. & Lou, X. W. D. Necklace-like structures composed of Fe₃N@C yolk-shell particles as an advanced anode for sodium-ion batteries. *Adv. Mater.* **30**, 1800525 (2018).
- Zhang, F. et al. Metallic porous iron nitride and tantalum nitride single crystals with enhanced electrocatalysis performance. *Adv. Mater.* **31**, e1806552 (2019).
- Huang, H. et al. Fe₃N constrained inside C nanocages as an anode for Li-ion batteries through post-synthesis nitridation. *Nano Energy* **31**, 74–83 (2017).
- Wei, S. et al. A stable room-temperature sodium-sulfur battery. *Nat. Commun.* **7**, 11722 (2016).
- Zhang, L. et al. Single nickel atoms on nitrogen-doped graphene enabling enhanced kinetics of lithium-sulfur batteries. *Adv. Mater.* **31**, 1903955 (2019).
- Li, R. et al. Sandwich-like catalyst-carbon-catalyst trilayer structure as a compact 2D host for highly stable lithium-sulfur batteries. *Angew. Chem., Int. Ed.* **59**, 12129–12138 (2020).
- Kresse, G. & Hafner, J. Ab initio molecular dynamics for liquid metals. *Phys. Rev. B* **47**, 558–561 (1993).
- Perdew, J. P., Burke, K. & Ernzerhof, M. Generalized gradient approximation made simple. *Phys. Rev. Lett.* **77**, 3865–3867 (1996).
- Blöchl, P. E. Projector augmented-wave method. *Phys. Rev. B* **50**, 17953–17979 (1994).
- Goedecker, S. Minima hopping: an efficient search method for the global minimum of the potential energy surface of complex molecular systems. *J. Chem. Phys.* **120**, 9911–9917 (2004).
- Larsen, A. H. et al. The atomic simulation environment—a Python library for working with atoms. *J. Phys.: Condens. Matter* **29**, 273002 (2017).
- Zhang, B. W. et al. Atomic cobalt as an efficient electrocatalyst in sulfur cathodes for superior room-temperature sodium-sulfur batteries. *Nat. Commun.* **9**, 4082 (2018).
- Wang, N. et al. High-performance room-temperature sodium-sulfur battery enabled by electrocatalytic sodium polysulfides full conversion. *Energy Environ. Sci.* **13**, 562–570 (2020).
- Bao, W. et al. Boosting performance of Na-S batteries using sulfur-doped Ti₃C₂Tx MXene nanosheets with a strong affinity to sodium polysulfides. *ACS nano* **13**, 11500–11509 (2019).
- Ye, C. et al. Electron-state confinement of polysulfides for highly stable sodium-sulfur batteries. *Adv. Mater.* **32**, 1907557 (2020).
- Xu, X. et al. A room-temperature sodium-sulfur battery with high capacity and stable cycling performance. *Nat. Commun.* **9**, 3870 (2018).
- Li, R., Zhou, X., Shen, H., Yang, M. & Li, C. Conductive holey MoO₂-Mo₃N₂ heterojunctions as job-synergistic cathode host with low surface area for high-loading Li-S batteries. *ACS nano* **13**, 10049–10061 (2019).
- Seh, Z. W., Sun, J., Sun, Y. & Cui, Y. A highly reversible room-temperature sodium metal anode. *ACS Cent. Sci.* **1**, 449–455 (2015).
- Di Lecce, D., Minnetti, L., Polidoro, D., Marangon, V. & Hassoun, J. Triglyme-based electrolyte for sodium-ion and sodium-sulfur batteries. *Ionics* **25**, 3129–3141 (2019).
- Chen, K. et al. Untying thioether bond structures enabled by “voltage-scissors” for stable room temperature sodium-sulfur batteries. *Nanoscale* **11**, 5967–5973 (2019).
- Kim, I. et al. A singular flexible cathode for room temperature sodium/sulfur battery. *J. Power Sources* **307**, 31–37 (2016).
- Lu, Q. et al. Freestanding carbon fiber cloth/sulfur composites for flexible room-temperature sodium-sulfur batteries. *Energy Storage Mater.* **8**, 77–84 (2017).
- Zhang, B. W. et al. Long-life room-temperature sodium-sulfur batteries by virtue of transition-metal-nanocluster-sulfur interactions. *Angew. Chem., Int. Ed.* **57**, 1–6 (2018).
- Zhang, L. et al. Self-assembling hollow carbon nanobeads into double-shell microspheres as a hierarchical sulfur host for sustainable room-temperature sodium-sulfur batteries. *ACS Appl. Mater. Interfaces* **10**, 20422–20428 (2018).
- Yang, T. et al. Design and construction of sodium polysulfides defense system for room-temperature Na-S battery. *Adv. Sci.* **6**, 1901557 (2019).
- Du, W. et al. Cobalt nanoparticles embedded into free-standing carbon nanofibers as catalyst for room-temperature sodium-sulfur batteries. *J. Colloid Interface Sci.* **565**, 63–69 (2020).
- Du, W. et al. Rational construction of rGO/VO₂ nanoflowers as sulfur multifunctional hosts for room temperature Na-S batteries. *Chem. Eng. J.* **379**, 122359 (2020).

62. Zha, C. et al. Facet-tailoring five-coordinated Ti sites and structure-optimizing electron transfer in a bifunctional cathode with titanium nitride nanowire array to boost the performance of Li_2S_6 -based lithium–sulfur batteries. *Energy Storage Mater.* **26**, 40–45 (2020).
63. Qiang, Z. et al. Ultra-long cycle life, low-cost room temperature sodium–sulfur batteries enabled by highly doped (N, S) nanoporous carbons. *Nano Energy* **32**, 59–66 (2017).
64. Wang, X., Zhang, Z., Qu, Y., Lai, Y. & Li, J. Nitrogen-doped graphene/sulfur composite as cathode material for high capacity lithium sulfur batteries. *J. Power Sources* **256**, 361–368 (2014).
65. Chen, Y.-M. et al. A nitrogen doped carbonized metal–organic framework for high stability room temperature sodium–sulfur batteries. *J. Mater. Chem. A* **4**, 12471–12478 (2016).
66. Zhang, Y. et al. Improvements in the electrochemical kinetic properties and rate capability of anatase titanium dioxide nanoparticles by nitrogen doping. *ACS Appl. Mater. Interfaces* **6**, 4458–4465 (2014).
67. Zhang, R. et al. A safe, low-cost, fast-kinetics and low-strain inorganic-open-framework anode for potassium-ion batteries. *Angew. Chem., Int. Ed.* **58**, 16474–16479 (2019).
68. Jin, F., Xiao, S., Lu, L. & Wang, Y. Efficient activation of high-loading sulfur by small CNTs confined inside a large CNT for high-capacity and high-rate lithium–sulfur batteries. *Nano Lett.* **16**, 440–447 (2016).
69. Gao, W., Wang, Z., Peng, C., Kang, S. & Cui, L. Accelerating the redox kinetics by catalytic activation of “dead sulfur” in lithium–sulfur batteries. *J. Mater. Chem. A*. <https://doi.org/10.1039/d1ta00772f> (2021).
70. Hwang, T. H., Jung, D. S., Kim, J. S., Kim, B. G. & Choi, J. W. One-dimensional carbon–sulfur composite fibers for Na–S rechargeable batteries operating at room temperature. *Nano Lett.* **13**, 4532–4538 (2013).
71. Yang, T. et al. A strategy for polysulfides/polyselenides protection based on $\text{Co}_9\text{S}_8/\text{SiO}_2/\text{C}$ host in Na– SeS_2 batteries. *Adv. Funct. Mater.* <https://doi.org/10.1002/adfm.202001952> (2020).
72. Waluś, S. et al. Lithium/sulfur batteries upon cycling: structural modifications and species quantification by in situ and operando X-ray diffraction spectroscopy. *Adv. Energy Mater.* <https://doi.org/10.1002/aenm.201500165> (2015).
73. Yu, S.-H. et al. Direct visualization of sulfur cathodes: new insights into Li–S batteries via operando X-ray based methods. *Energy Environ. Sci.* **11**, 202–210 (2018).
74. Li, W. et al. The synergetic effect of lithium polysulfide and lithium nitrate to prevent lithium dendrite growth. *Nat. Commun.* **6**, 7436 (2015).
75. Zheng, J. et al. Lewis acid–base interactions between polysulfides and metal organic framework in lithium sulfur batteries. *Nano Lett.* **14**, 2345–2352 (2014).
76. Zhao, C.-Z. et al. Li_2S_5 -based ternary-salt electrolyte for robust lithium metal anode. *Energy Storage Mater.* **3**, 77–84 (2016).
77. Wu, F. et al. Boosting high-performance in lithium–sulfur batteries via dilute electrolyte. *Nano Lett.* **20**, 5391–5399 (2020).
78. Wang, Z. et al. An anionic-MOF-based bifunctional separator for regulating lithium deposition and suppressing polysulfides shuttle in Li–S batteries. *Small Methods* **4**, 2000082 (2020).

Acknowledgements

We appreciate support from National Natural Science Foundation of China (No. 22005251, No. 22179109), Chongqing Natural Science Foundation (cstc2020jcyj-bshX0047, cstc2020jcyj-zdxmX0010), Central Universities Fundamental Research Funds (XDJK2020C004, XDJK2019AA002).

Author contributions

Y.Q. designed this work, synthesized the sample, analyzed the data, and wrote the paper; Q.-J.L. performed the theoretical calculation, analyzed the data, and revised the manuscript; Y.C., M.X., and G.W. provided sources, supervised the work, and revised the manuscript; Y.W., S.B., and C.L. participated the discussion.

Competing interests

The authors declare no competing interests.

Additional information

Supplementary information The online version contains supplementary material available at <https://doi.org/10.1038/s41467-021-26631-y>.

Correspondence and requests for materials should be addressed to Yuming Chen, Guoxiu Wang or Maowen Xu.

Peer review information *Nature Communications* thanks Sundara Ramaprabhu, and the other, anonymous, reviewer(s) for their contribution to the peer review of this work. Peer reviewer reports are available

Reprints and permission information is available at <http://www.nature.com/reprints>

Publisher's note Springer Nature remains neutral with regard to jurisdictional claims in published maps and institutional affiliations.



Open Access This article is licensed under a Creative Commons Attribution 4.0 International License, which permits use, sharing, adaptation, distribution and reproduction in any medium or format, as long as you give appropriate credit to the original author(s) and the source, provide a link to the Creative Commons license, and indicate if changes were made. The images or other third party material in this article are included in the article's Creative Commons license, unless indicated otherwise in a credit line to the material. If material is not included in the article's Creative Commons license and your intended use is not permitted by statutory regulation or exceeds the permitted use, you will need to obtain permission directly from the copyright holder. To view a copy of this license, visit <http://creativecommons.org/licenses/by/4.0/>.

© The Author(s) 2021